STUDENTSKÁ PŘEHLÍDKA

S1

XAFS STUDY OF MN-DOPED Bi_2Se_3 AND Bi_2Te_3 TOPOLOGICAL INSULATORS

J. Růžička[1], O. Caha[1], V. Holý[2], G. Springholz[3], H. Steiner[3] and G. Bauer[3]

[1]Department of Condensed Matter Physics and CEITEC, Masaryk University, Kotlářská 2, 611 37 Brno, Czech Republic
[2]Department of Electronic Structures, Charles University, Praha, Czech Republic
[3]Institut für Halbleiter- und Festkörperphysik, Johannes Kepler Universität, Altenbergerstrasse 69, 4040 Linz, Austria
ruzmen@physics.muni.cz

Keywords: topological insulators, magnetic doping, dopant position determination

Abstract

We study incorporation of Mn atoms into the lattice of topological insulators Bi_2Se_3 and Bi_2Te_3 grown by MBE on BaF_2 substrate. X-ray absorption fine structure around Mn K edge was measured and first coordination shell fits were made in order to investigate the nearest neighbours of Mn atoms. While in Bi_2Te_3 Mn atoms occupy distorted octahedral positions between Te layers, in the case of Bi_2Se_3 none of expected positions resulted in a good fit.

Introduction

Topological insulators attracted a lot of attention in recent years. While in the bulk they behave like ordinary insulators, their surface states are quite extraordinary. The 2D topological surface states have a conical energy-momentum dispersion and spins of electrons are locked to their momentum. Also due to time reversal symmetry the spins are protected from flipping. Such properties promise many applications in spintronics and quantum computing. Doping topological insulators by magnetic ions opens a gap in the energetic structure and allows for long-range magnetic order, thus further increasing possibilities of application [1].

Among the most studied topological insulators are Bi_2Se_3 and Bi_2Te_3. Both materials have hexagonal structure of R3m symmetry. The unit cell consists of 15 atomic layers grouped in three quintuplets with Se/Te–Bi–Se/Te–Bi–Se/Te order (see Fig. 1a). The quintuplets are van der Waals bonded to each other by a double layer of Se/Te atoms – so-called van der Waals gap [1]. Because this gap is bigger than other interlayer distances in the structure, it is expected to host extrinsic atoms in the case of doping. There are two possible symmetric positions within the gap – distorted octahedral and distorted tetrahedral site, in both cases surrounded by Se/Te atoms (see Fig. 1b). Other possibility is that extrinsic atoms substitute Bi.

Experiment

The studied epitaxial layers of Bi_2Se_3 and Bi_2Te_3 were grown by MBE on cleaved BaF_2 substrates at substrate temperature 300–400 °C. The quality of the layers was monitored in-situ by RHEED.

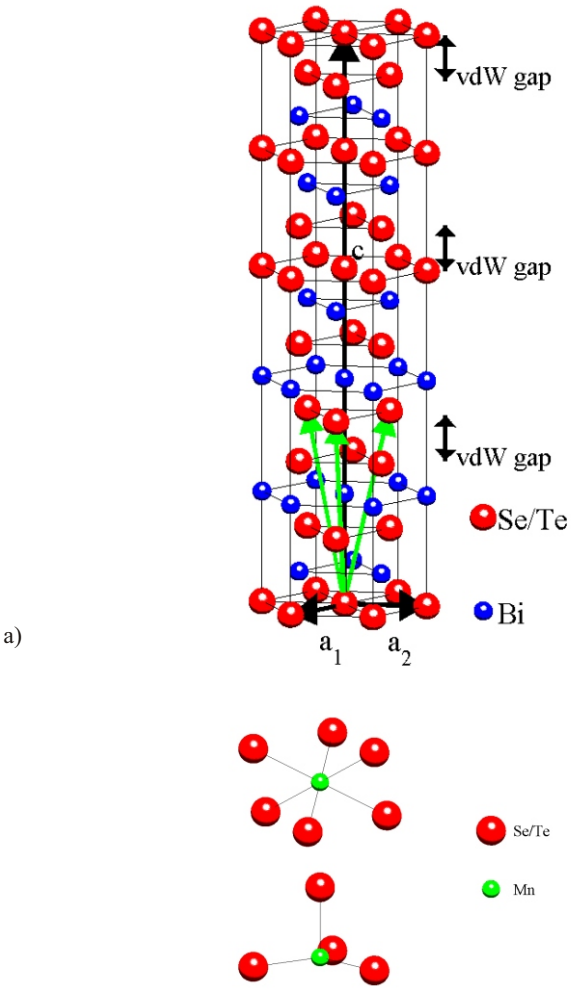

Figure 1. a) Hexagonal unit cell of Bi_2Se_3 and Bi_2Te_3 consisting of three quintuplets of atomic layers connected by van der Waals gaps. Basis vectors are in black, green arrows form an alternative rhombohedral basis. b) Possible positions of Mn atoms within the van der Waals gap – distorted octahedral (top) and distorted tetrahedral (bottom).

The X-ray absorption fine structure (XAFS) spectra were obtained at beamline BM23 of ESRF, Grenoble at Mn K edge (6539 eV). Samples were measured with incident angle 2.5°. The detected signal was fluorescence radiation.

Results

Measured data were processed by Athena and fitting was performed using Artemis [2]. Theoretical spectra calculations were done by FEFF9 [3].

Bi_2Se_3

Measured data and the Fourier transforms for different Mn concentrations follow in Fig. 2.

Nearest neighbor distance can be estimated from the position of the first coordination shell peak of the Fourier transform; for Bi_2Se_3 they are summarized in Tab. 1.

First calculations were made for three expected possible positions of Mn – octahedral and tetrahedral interstitial positions in the van der Waals gap and substitutional position at Bi site. Resulting spectra are compared with one of the measurements in Fig. 3. It is quite clear that none of the suggested positions matches the measurement. Trying to fit these models to the data produced no physically sound results.

We have tried also combinations of the various Mn positions in the Bi_2Se_3 lattice, but to no success so far. A very characteristic feature of the measured spectra is the peak triplet near the edge, which we could not sufficiently reproduce.

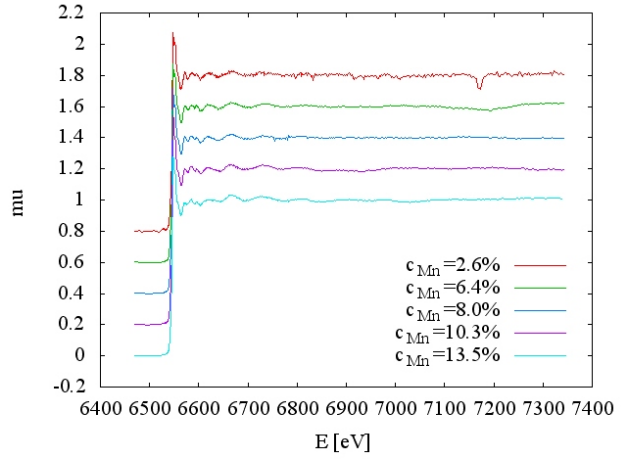

a)

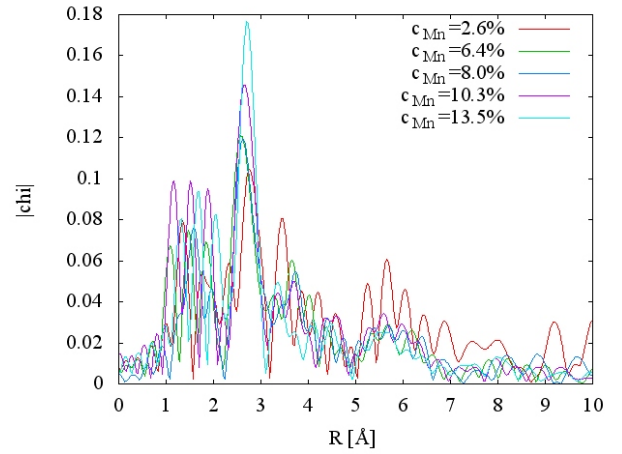

b)

Figure 2. a) Measured XAFS spectra of Mn-doped Bi_2Se_3 at Mn K edge, b) Fourier transforms.

Table 1. Nearest neighbour distances in Mn-doped Bi_2Se_3

nominal Mn concentration [%]	nearest neighbour distance estimate [Å]
2.6	2.76 ± 0.03
6.4	2.58 ± 0.03
8.0	2.61 ± 0.03
10.3	2.67 ± 0.03
13.5	2.70 ± 0.03

Bi_2Te_3

Measured data and their Fourier transforms for different Mn concentrations follow in Fig. 4, nearest neighbour distances estimated from the first shell peak can be found in Tab. 2.

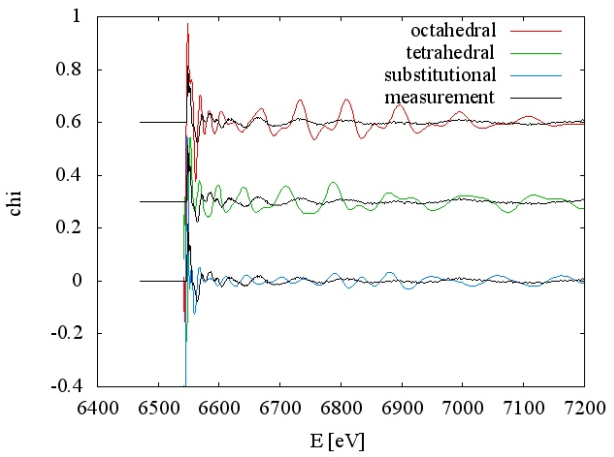

Figure 3. Comparison of measured and calculated spectra of Mn-doped Bi_2Se_3. Sample with Mn concentration 10.3%, calculation for three expected possible positions of Mn.

We started again by calculating spectra of the three expected positions (see Fig. 5). In this case the octahedral position matches the measurement quite well. Data of the sample with lowest Mn concentration have a limited *k*-range because of artifact at about 6900 eV and the Fourier transform is therefore featureless and the fitting parameters have too large errors. Sample with 4% of Mn also couldn't be fitted, in this case due to many small glitches in the data. However the other three samples were fitted nicely, see for example Fig. 6. The model used contained the nearest six Te atoms and the two nearest Bi atoms. Resulting nearest neighbor distances are in Tab. 2.

Conclusion

We have successfully determined that in the case of Bi_2Te_3 Mn atoms are incorporated in octahedral positions within the van der Waals gap. In the case of Bi_2Se_3 none of the expected positions corresponds to the data and none of our attempts with combinations of the positions was successful.

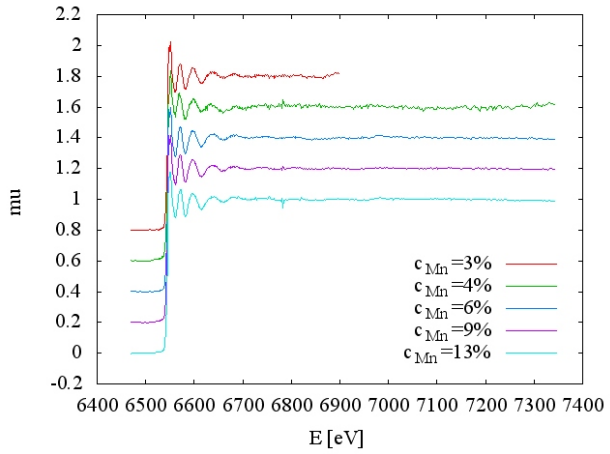

a)

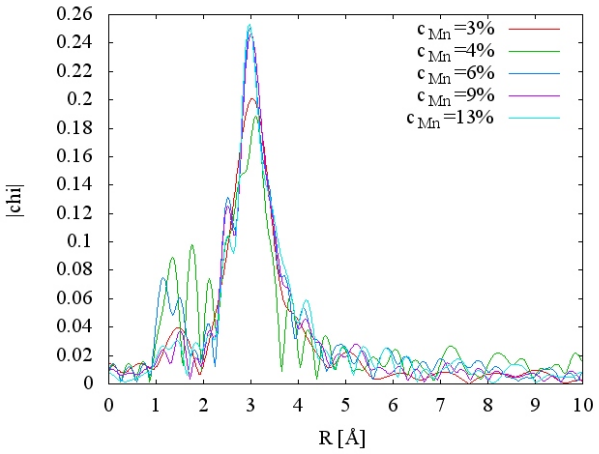

b)

Figure 4. a) Measured XAFS spectra of Mn-doped Bi_2Te_3 at Mn K edge, b) Fourier transforms.

We hope further work will lead to successful determination also in this case.

References

1. O. Caha, A. Dubroka, J. Humlíček, V. Holý, H. Steiner, M. Ul-Hassan, J. Sánchez-Barriga, O. Rader, T. N. Stanislavchuk, A. A. Sirenko, G. Bauer and G. Springholz, accepted to *Crystal Growth & Design*, DOI 10.1021/cg400048g.
2. B. Ravel and M. Newville, *Journal of Synchrotron Radiation*, **12**, 2005, p. 537.
3. J. J. Rehr, J. J. Kas, M. P. Prange, A. P. Sorini, Y. Takimoto, F. D. Vila, *Comptes Rendu Physique*, **10**, 2009, p. 548.

Acknowledgements

The work was supported by the CSF project P204/12/0595. We thank Cornelius Strohm for assistance at beamline BM23 of ESRF synchrotron. ESRF participation is supported by INGO LA10010 project.

Table 2. Nearest neighbour distances in Mn-doped Bi_2Te_3

nominal Mn concentration [%]	n. n. distance estimate [Å]	n. n. distance from fit [Å]
3	3.04 ± 0.03	-
4	3.10 ± 0.03	-
6	2.98 ± 0.03	2.916 ± 0.008
9	3.01 ± 0.03	2.918 ± 0.008
13	2.98 ± 0.03	2.91 ± 0.01

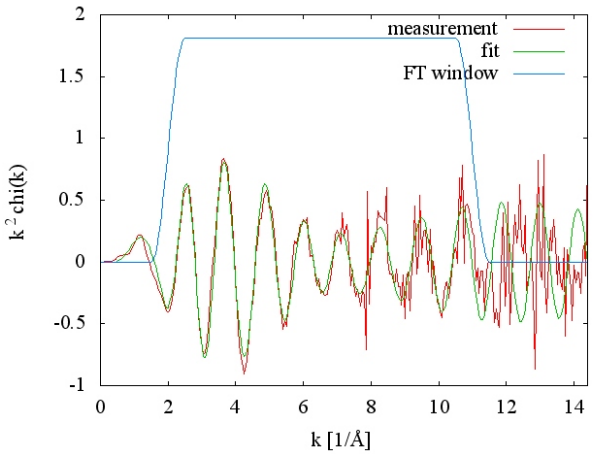

a)

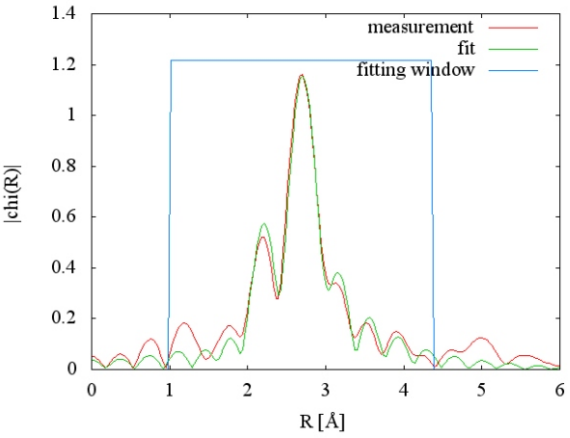

b)

Figure 6. Best fit for sample with Mn concentration 9%. a) *k*-space, b) *R*-space.

S2

KINETIC MONTE CARLO SIMULATION OF GROWTH OF Ge QUANTUM DOT MULTILAYERS WITH AMORPHOUS MATRIX

J. Endres[1], S. Daniš[1], V. Holý[1], M. Mixa[1], M. Buljan[2]

[1]*Charles University in Prague, Faculty of Mathematics and Physics, Prague, Czech Republic*
[2]*Rudjer Boskovic Institute, Zagreb, Croatia*
endres.jan@google.com

Quantum dot (QD) multilayers with amorphous matrix are intensively studied because of their physical properties. Due to the size of QDs many quantum effects are observable for these systems, what can be used for many technical applications. Possible applications of QD multilayers are lasers, solar cells, photodetectors or high-speed memories.

Former studies were focused on systems with crystalline matrix [1, 2]. These systems are predominantly prepared by Stranski-Krastanow growth. At first thin strained wetting layer is grown, until it is energetically preferred to relieve elastic energy by creating QDs. The cover layer is then deposited onto the QD layer and the growth can continue with other wetting layer.

QD multilayers with amorphous matrix are mainly prepared by deposition on substrate via magnetron sputtering [3-6]. Samples consist of altering layers of QDs and matrix material. QDs layer is deposited first (material of QDs can be deposited in the same time as matrix material). Then this deposited layer is overlaid by cover layer consisting only matrix material.

Self-ordering of QDs was observed in both types of systems [1-6]. The ordering in multilayer originates in preferential nucleation of QDs during the growth in the minima of the chemical potential (i.e. surface energy) on the surface of the cover or wetting layer. In the case of the systems with crystalline matrix the driving force for self-ordering is elastic strain field originates from mismatch of lattices of materials in wetting and cover layers. However, there is no strain in multilayers with amorphous matrix. In such systems self-ordering is caused only by surface morphology of the cover layers. Two types of stacking of neighbouring layers of QDs (ABC, ABA) were observed in systems of Ge QDs in different amorphous matrix (SiO_2, resp. Al_2O_3), see [4-6]. Finding the conditions which leads to these types of stacking was target of performed simulations.

Chemical potential at point on surface $\boldsymbol{x} = (x,y)$ is given as [7]

$$(x) \quad _0 \quad w(\boldsymbol{x})V_0 \qquad (\boldsymbol{x})V_0 \tag{1}$$

where is a constant reference value of the chemical potential, w is the volume density of elastic energy, is the surface tension, is the surface curvature and V_0 is the atomic volume. Due to the amorphous matrix there is no strain in the multilayer and the second term in equation (1) is thus zero and chemical potential depends only on the curvature (i.e. morphology) of the surface of cover layer.

We consider that the surface shape is originated from deposition of cover layer over the QDs when a hill of material is created above each QD. Multilayer and dots can be described by three indexes j_1, j_2, j_3. Index j_3 denotes the position of layer in the z axis direction with zero at substrate and oriented to sample surface. This index is used for both dot and corresponding cover layer. Indexes j_1 and j_2 then label dots in x and y axes direction in the given layer j_3. For the shape of these hills on the surface of cover layer j_3 we use function [4]

$$h_{j_3} \qquad _{j_1 j_2} \quad f(\boldsymbol{x} \quad \boldsymbol{X}_{j_1 j_2 j_3 \ 1}) \quad Cf(\boldsymbol{x} \quad \boldsymbol{X}_{j_1 j_2 j_3 \ 2}) \tag{2}$$

where $\boldsymbol{x} = (x,y)$ is point on surface, $\boldsymbol{X}_{j1,j2,j3\text{-}1}$ and $\boldsymbol{X}_{j1,j2,j3\text{-}2}$ are positions of QDs in layers j_3-1 and j_3-2, parameter C is inheritance factor which determines the contribution of height of interlayer surface above QDs layer j_3-2 and f($\boldsymbol{x}$) is Gauss function

$$f(x) \quad \exp \quad \frac{|x|^2}{2 \ ^2} \tag{3}$$

where is a parameter determining full width at half maximum. When inheritance factor C is greater than 0, surface height is affected not only by last layer but also by one lower layer, which can cause ordering of QDs in vertical direction.

Simulation of the growth can be performed by Kinetic Monte Carlo (KMC) method. Simulation model was based on several processes which can occur [2]. The adatoms can be deposited onto the surface, adatoms can diffuse on it, adatoms can join into the QD or can escape it. Adatoms are moving by thermally activated hopping between neighboring sites of square discrete simulation lattice. The size of the whole lattice has to be big enough to not be affected by edge effects of finite-size simulation lattice. Periodic boundary conditions are considered during simulation, so if some adatom leaves the simulation area, it reappears on the opposite side. After the completed growth of actual layer the surface of cover layer was computed as hills (defined by analytical functions) over buried dots. This surface shape was used to determine the curvature chemical potential which serves as driven force for simulation of next layer [4].

To analyze the correlation of distances between QDs in lateral direction we used the radial distribution function (RDF). It describes the probability of finding the center of a particle at given lateral distance from the center of another particle. This function can be evaluated for QDs in one layer to determine the lateral ordering in one layer or between chosen layer l and next three layers j + 1,2,3 to determine the ordering of the dots in vertical direction (type of layers stacking, ABC or ABA).

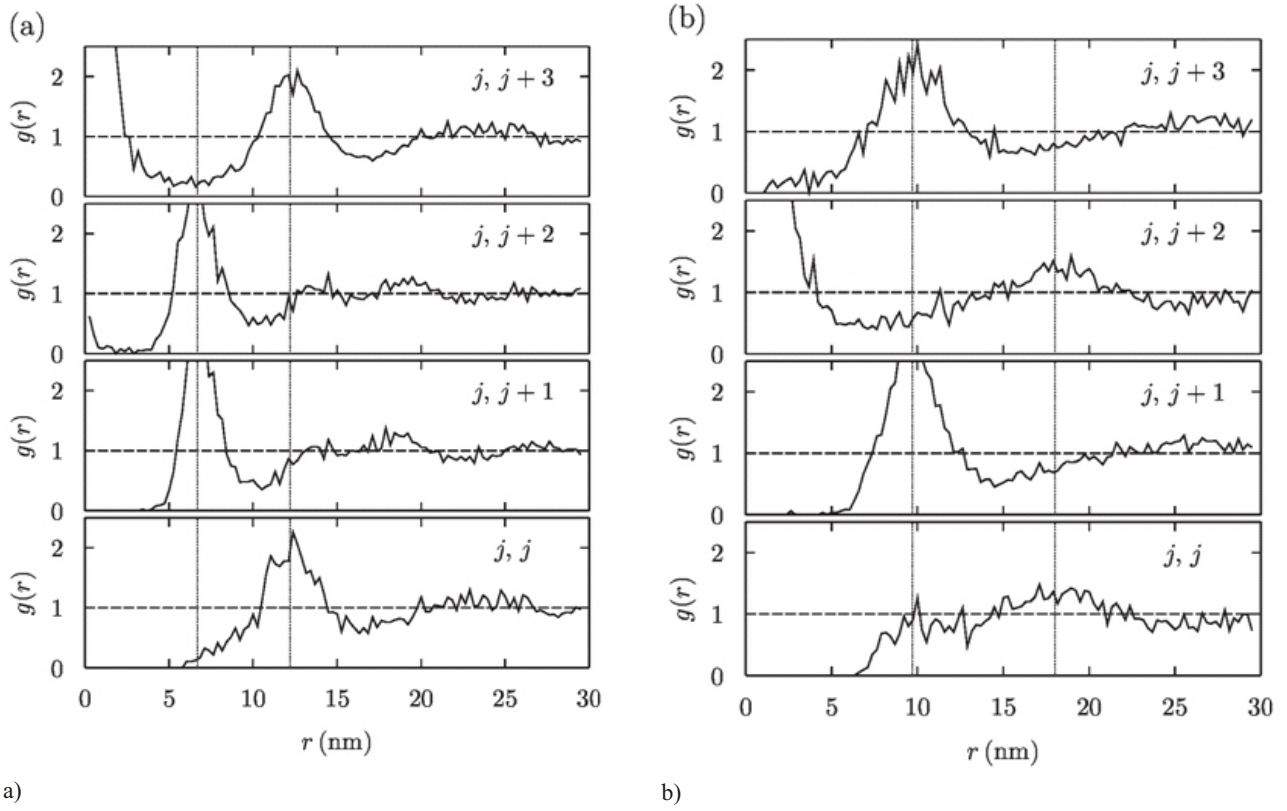

a) b)

Figure 1. Radial distribution functions for dots in layer $j = 20$ and dots in layers j, j+1, j+2, j+3 for system with (a) inheritance factor $C = 0.5$ and narrower Gauss functions of surface shape and (b) $C = 0.0$ and broader Gauss functions for determining the shape of cover layer surface. Value of 1 (value in the infinity distance) is marked by dashed line and positions of maxima determining the distance of nearest neighbor dots by dotted line. Positions of maxima reveal that in case (a) the stacking order of the layers is ABC and in the case (b) it is ABA. For detailed description see the text.

In the case of partially ordered layer of QDs the RDF should have the first highest maximum at the position r_m, which correspond with the distance of the first shell of dots around the center dot and can be considered as the most probable distance between all neighbouring dots. In dependence of the degree of ordering, we can seed other lower maximums, which correspond with next shells of dots.

In the case of ABA stacking QDs in layer j+2 is aligned above dots in layer j, for ABC type stacked layers j + 1,2 are offset and layer j + 3 is aligned above dots in layer j. So the ABC stacking correspond with the first maximum of RDF for layer j + 1,2 at about one half of distance r_m. The maximums of RDF for layer j + 3 are at 0 and at r_m again. In the case of ABA stacking the first maximum of RDF for layer j + 1 is at about one half of r_m and maximums for layer j + 2 are at 0 and r_m.

In performed simulations we observed the short-range lateral self-ordering in particular layers. This ordering (with size of the dots and distance between them) can be influenced by parameters of deposition, like temperature, deposition flux or volume of deposited material. The ordering in vertical direction can be tuned by changing of properties of surface morphology, e.g. the parameters of functions describing the hills over dots like width or inheritance factor.

The different types of stacking order of quantum dot layers (ABC or ABA) were observed, see Fig. 1. RDF corresponding with ABC stacking is in Fig. 1(a). As was mentioned above we see maximum in RDF of positions of dots in layer $j = 20$ at distance approximately $r_m = 12$ nm. For RDF for dots between layers j and j + 1,2 we see maxim at approximately 7 nm. And for RDF for dots between layers j and j+3 we see maxima at 0 and 12 nm. RDF corresponding with ABA stacking is in Fig. 1(b). Maximum in RDF of positions of dots in layer $j = 20$ at distance approximately $r_m =$ 18 nm. Maximum at the same position is also in part of RDF for layer j + 2 (he we see maximum at 0 too). Maxima at approximately 10 nm are visible at RDF for layers j + 1,2.

1. J. Stangl, V. Holý, G. Bauer, *Rev. Mod. Phys.*, **76**, (2004), 725.
2. M. Mixa, V. Holý, G. Springholz, G. Bauer, *Phys. Rev. B*, **80**, (2009), 045325.
3. M. Buljan, U. V. Desnica, G. Dražić, M. Ivanda, N. Radić, P. Dubček, K. Salamon, S. Bernstorff, V Holý, *Nanotechnology*, **20**, (2009), 085612.
4. M. Buljan, U. V. Desnica, M. Ivanda, N. Radić, P. Dubček, G. Dražić, K. Salamon, S. Bernstorff, V. Holý, *Phys. Rev. B*, **79**, (2009), 035310.
5. M. Buljan, S. R. C. Pinto, A. G. Rolo, J. Martínn-Sanchez, M. J. Gomez, J. Grenzer, A. Mücklich, S. Bernstorff, V. Holý, *Phys. Rev. B*, **82**, (2010), 235407.
6. M. Buljan, N. Radić, M. Ivanda, I. Bogdanović-Radović, M. Karlušić1, J. Grenzer, S. Prucnal, G. Dražić, G. Pletikapić, V. Svetličić, M. Jerčinović, S. Bernstorff, and V Holý, *J. Nanopart. Res.*, **15**, (2013), 1485.
7. H. Gao, *J. Mech. Phys. Solids*, **42,** (1994), 741.

S3

STRUCTURAL PROPERTIES OF EPITAXIAL Ge MICROCRYSTALS ON SI

J. Rozbořil[1], M. Meduňa[1], C.V. Falub[2], F. Isa[3], G. Isella[3], H. von Känel[2]

[1]Department of Condensed Matter Physics & CEITEC, Masaryk University, Kotlářská 2, 61137 Brno, Czech Republic

[2]Laboratory for Solid State Physics, ETH-Zürich, Schafmattstrasse 16, 8093 Zürich, Switzerland [3]L-NESS, Department of Physics, Politecnico di Milano, via Anzani 42, 22100 Como, Italy

357604@mail.muni.cz

The fabrication of modern semiconducting optical devices requires combining of different materials. Heteroepitaxial growth of layers with different lattice parameters and thermal expansion coefficients generates many obstacles during fabrication, in particular, creation of misfit and threading dislocations in the deposited layer and cracks, which detrimentally affect the fabricated device. One of the main applications of Ge/Si heteroepitaxial thick layers can be a development of new generation of x-ray detectors.

Successful method of fabricating defect-free epitaxial Ge/Si layers involves patterning of the Si substrate into periodic arrays of pillars by a conventional photolithography and deep reactive ion etching, on which germanium layer is deposited by Low-Energy Plasma-Enhanced Chemical Vapor Deposition (LEPECVD) at high growth rate [1]. Separated relaxed Ge microcrystals with defects localized only in a small area around Ge/Si interface, which doesn't affect bulk properties, can be a solution (Fig. 1). The crystals can be grown up to height of several tens of micrometers and the material deposited can result in space filling even up to 96 % of surface.

Series of Ge microcrystal samples grown on Si substrate with different structure parameters were studied by high-resolution x-ray diffraction technique using reciprocal space mapping around symmetrical (004) and asymmetrical (224) diffractions. We have used home assembled diffractometer with a Cu x-ray tube equipped with a 4-bounce Ge(220) crystal monochromator on the incident beam and an analyzer crystal on the diffracted beam, providing CuK $_1$ radiation.

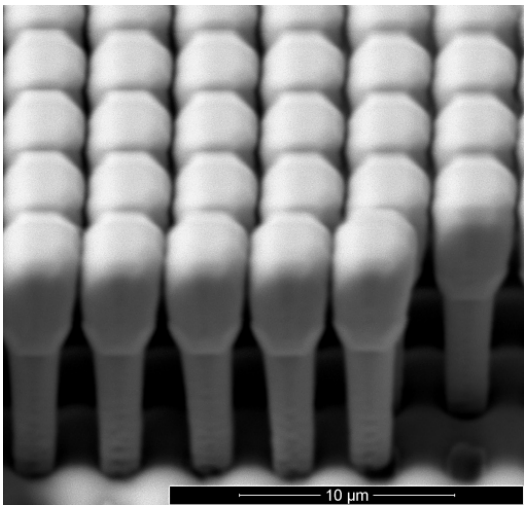

Figure 1. Perspective view SEM micrograph of 8 □m tall Ge microcrystals grown on Si substrate with 8 □m tall and 2 □m wide pillars, spaced by 2 □m gaps.

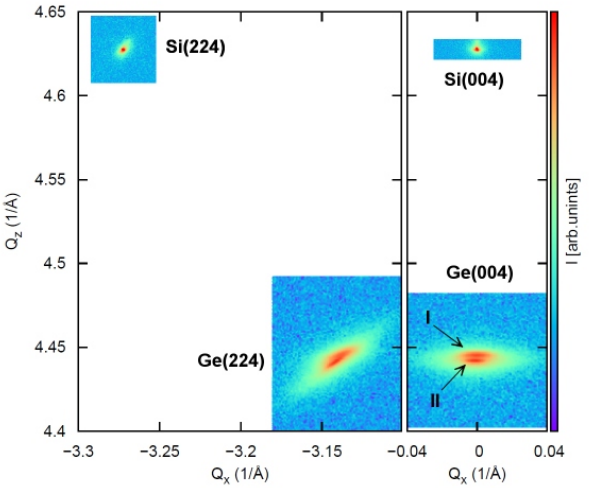

Figure 2. Reciprocal space maps around 224 (left) and 004 (right) diffractions for sample of 3 m tall Ge microcrystals grown on Si substrate with 8 m tall and 2 m wide pillars, spaced by 3 m gaps. Peak I-strained Ge between pillars; peak II-relaxed Ge towers.

Two significant Ge diffraction peaks on the measured maps are clearly observed (Fig. 2). The first one refers to strained germanium deposited inside the trenches between the Si pillars and the second one refers to germanium deposited on the top of the Si pillars, which is completely relaxed. The intensity of both kinds of peaks and also their width strongly depend on the structure of the samples, patterning, height etc.

Particularly in this study we compare samples which differ from each other in Ge crystal height, size of the Si pillars and distances between them. The Ge crystal height varies in the range from 1 to 30 m. The Si pillars on a substrate have square cross-section and they are arranged in a square grid. The Si pillars are 8 m tall on all samples, their widths are in the range from 2 to15 m and they are spaced with the gaps varying from 1 to 50 m. The crystal lattice properties such as lattice parameter, tilt, strain and degree of relaxation and their dependence on the sample patterning were studied using intensity, FWHM and position of diffraction peaks.

1. C.V. Falub, H. von Känel, F. Isa, R. Bergamaschini, A. Marzegalli, D. Chrastina, G. Isella, E. Müller, P. Niedermann, L. Miglio, Science, 335, (2012), 1330-1334.
2. C. V. Falub, M. Meduna, D. Chrastina, F. Isa, A. Marzegalli, T. Kreiliger, A.G. Taboada, G. Isella, L. Miglio, A. Dommann, and H. von Kanel, Scientific Reports **3** (2013), 2276.

S4

Fe_2O_3/TiO_2 NANOPARTICLES - A COMPLEX STRUCTURAL STUDY

V. Valeš[1], M. Buljan[2], S. Bernstorff[3], S. Mangold[4], V. Holý[1]

[1]*Faculty of Mathematics and Physics, Charles University, Ke Karlovu 5, 121 16 Praha, Czech Republic*
[2]*Ruder Bošković Institute, Bijeni?ka cesta 54, 10000 Zagreb, Croatia*
[3] *Elettra - Sinctrotrone Trieste S. C. p. A., Strada Statale 14, 34149 Basovizza, Italy*
[4] *ANKA Synchrotron Radiation Facility, KIT, Hermann-von-Helmholtz-Platz 1, D-76344 Eggenstein-Leopoldshafen, Germany*
vales@mag.mff.cuni.cz

Titania (TiO_2)-based systems have been very intensively studied in last decades because of their photocatalytic activity, which found broad commercial applications [1]. Functionalized titania composites, especially Fe_2O_3/TiO_2 systems attracted a lot of attention recently, since they make it possible to improve the photocatalytic performance of titania [2]. The -phase of Fe_2O_3 exhibits a very large magnetic coercivity at room temperature so that Fe_2O_3/TiO_2 in solutions can easily be manipulated by external magnetic field. Fe_2O_3/TiO_2 compact thin layer composites as a photocatalyst can respond to visible light due to the narrow band-gap of Fe_2O_3. The optical and electronic parameters of Fe_2O_3/TiO_2 nanoparticles substantially depend on the width of their size distribution.

In our previous work [3] we dealt with semiconductor nanoparticles in amorphous silica matrix and we demonstrated that a self-ordering mechanism of the nanoparticles occurs during the deposition of multilayers. A spontaneous ordering of nanoparticles resulted in narrowing of the particle size distribution. In this work we use this approach for the improvement of the structure of Fe_2O_3/TiO_2 nanoparticle systems, namely we study the growth of $(Fe_2O_3+TiO_2)/SiO_2$ multilayers and the crystallization of the mentioned nanoparticles during post-growth annealing. We investigated the ordering and the size distribution of the particles using grazing-incidence small-angle X-ray scattering (GISAXS) and the inner crystalline structure by X-ray diffraction (XRD) and x-ray absorption spectroscopy (EXAFS).

The studied $(Fe_2O_3 + SiO_2)/(TiO_2 + SiO_2)/SiO_2$ samples were grown by a sequential deposition, in which 10-period multilayers (with a layers thickness 0.6, 1 or 2 nm and the SiO_2 spacer thickness of 10 nm) were deposited by electron beam evaporation onto rotating Si substrates at room temperature. The deposition rates were 10 Å/s for SiO_2 and 1 Å/s for both Fe_2O_3 and TiO_2. The samples have been subsequently annealed for 1 h at various temperatures in vacuum, air or forming gas (FG - Ar + 4% H_2). The partial results have already been published [4].

The powder xrd curves have been measured by a laboratory diffractometer with a standard X-ray tube (CuK , 1.4 kW). We used a parallel-beam setup with a parabolic multilayer mirror in the primary beam and a parallel-plate collimator and a flat graphite monochromator (to reduce the fluorescence signal from Fe atoms) in the diffracted beam. The angle of incidence of the primary beam was kept constant at 0.5 deg to suppress the substrate signal. Small angle grazing incidence X-ray scattering has been carried out at ELETTRA synchrotron at the SAXS beamline with the photon energy of 8 keV. The incidence angle was a few tenths deg above the critical angle of total external reflection. The scattered radiation was recorded by MAR image plate (2000 2000 pixels). The necessary angular resolution was achieved by a large sample-detector distance of about 1.9 m; the air scattering was suppressed by an evacuated flight-tube. The X-ray absorption spectroscopy has been performed at XAS beamline at ANKA synchrotron. We measured the spectra in the range 150 eV below and 650 eV above the absorption edge of both Fe and Ti in the fluorescence mode. The measured data have been processed and analyzed by the standard software package of the programs *Athena* and *Artemis*.

The xrd data show clearly visible peaks corresponding to the rutile-TiO_2. An example of the evolution of the crystallinity with annealing temperature of the samples with the layer thickness of 2 nm annealed in the air is displayed in the Fig. 1(a). The crystallite size obtained by the Sherrer equation applied to the 110 rutile peak exhibits a systematic growth with annealing temperature ranging from 4 nm at 700 C to 13 nm at 1000 C. For the sample annealed at the highest temperature, additional peak, which may correspond to hematite-Fe_2O_3, arises.

The findings from the xrd data have been validated by the EXAFS measurements. The absorption spectra around Ti edge revealed the presence of rutile-TiO_2 as expected. From the measurements around Fe edge we supposed to get information on the local structure around Fe atoms that we did not obtain form the xrd. The data were simulated with a model assuming that the sample consists of two components. The first component is one shell of octahedrally coordinated oxygen atoms around an iron atom and the second one is two-shell hematite structure. We observed a systematic increase of the two-shell component at the expense of simple octahedrons.

The measured GISAXS maps have been compared to the simulations carried out by our software using a model of disordered particles in a hexagonal two-dimensional array including interface roughness. Individual layers are expected to be laterally fully disordered due to the fact that the particles grow during annealing after multilayer growth. An example of nicely ordered particles (expressed by well-defined lateral maxima in the GISAXS map) is displayed in the Figure 1(b). The results from the GISAXS maps simulations show that with increasing annealing temperature particle size increases as well as the degree of ordering. At the temperature of 1000 C the particle

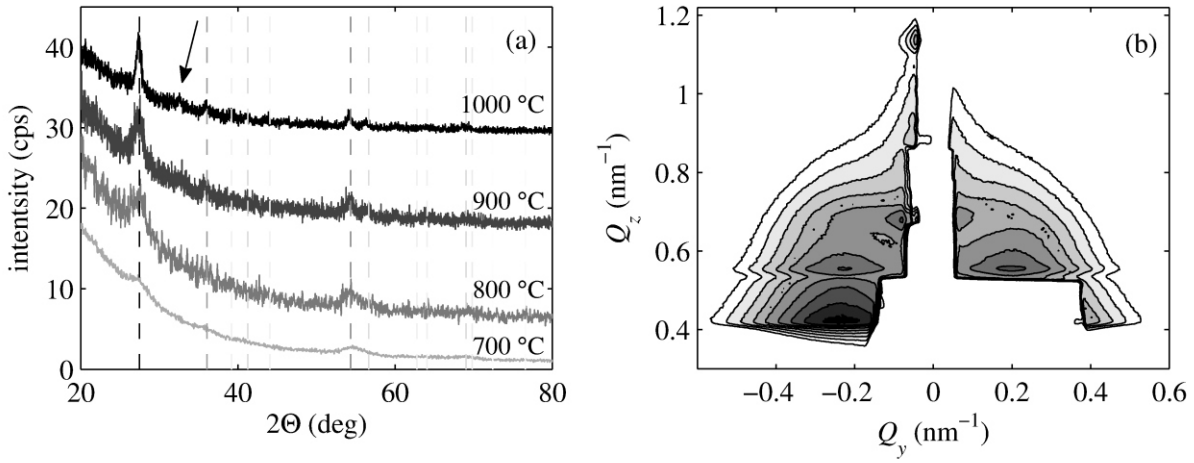

Figure 1. The evolution of diffraction profiles of samples annealed in the air (a) with diffraction peaks corresponding to rutile (the dashed lines, the grey scale corresponds to the relative peak intensity). The arrow denotes an additional peak corresponding to hematite-Fe_2O_3. In the panel (b) the GISAXS map in the logarithmic scale with the contour step of $10^{0.15}$ from sample annealed in the air at 900 C is displayed.

arrangement as well as inter-layer structure is broken, probably due to coalescence of particles from different layers. The particle sizes obtained from GISAXS are in the agreement with those obtained from xrd.

From the analysis of all the data from all experiments we found out that titanium oxide tends to form ordered rutile particles from the annealing temperature of 700 C with increasing crystallinity and better ordering for higher temperatures. The particles are smaller and closer together for thinner samples and vice versa. The multilayer structure is preserved up to temperatures around 900 C. On the other hand, iron atoms form only very small particles that are not recognizable by xrd and most of the atoms is surrounded only by octehdrally coordinated oxygen atoms. The best arrangement of (rutile) particles has been achieved for the sample annealed at 900 C in the air.

1. M. Hoffmann, S. Martin, W. Choi, D. Bahnemann, *Chemical Reviews*, **95**, (1995), 69.
2. H. Cui, W. Ren, W. Wang, *Journal of Sol-Gel Science and Technology*, **58**, (2011), 476.
3. M. Buljan, U. Desnica, M. Ivanda, N. Radić, P. Dubček, G. Dražić, K. Salamon, S. Bernstorff, V. Holý, *Physical Review B*, **79**, (2009), 035310.
4. V. Valeš, V. Holý, M. Buljan, V. Janicki, S. Bernstorff, *Thin Solid Films*, **520**, (2012), 4800.Review B, 79, (2009), 035310.

S5

STUDY OF HIGH TEMPERATURE PHASE OF TITANATE NANOTUBES

Tereza Brunatova[1], Daniela Popelkova[2], Peter Oleynikov[3], Stanislav Danis[1], Xiaodong Zou[3], Radomir Kuzel[1]

[1]Charles University, Faculty of Mathematics and Physics, Dept.of Condensed Matter Physics, Prague, Czech Republic
[2]Institute of Macromolecular Chemistry, Academy of Sciences of the Czech Republic, Prague, Czech Republic
[3]Berzelii Center EXSELENT on Porous Materials,Stockholm University, Dept. of Materials and Environmental Chemistry, Stockholm University, SE-106 91 Stockholm, Sweden

Titanate nanotubes (Ti-NT) are very promising material with many possible applications in bionedicine, in solar cells, lithium batteries, fuel cells etc [1]. Their structure is not fully undertood and there exists several possible stuctures of Ti-NT [1]. The study of temperature stability of Ti-NT is important because some of possible applications of Ti-NT require heating [1]. By heating of Ti-NT titanate nanowires are obtained. Similarly to Ti-NT several possible phases of titanate nanowires can be discovered as for example: $Na_2Ti_6O_{13}$ [2], $Na_2Ti_3O_7$ [2], rutile phase of TiO_2 [2-4], anatase phase of TiO_2 [2], [3], beta TiO_2 [4]. The final structure depends also on the amount of sodium ions if some are present in original Ti-NT sample.

In this contribution, the structure of Ti-NT the structure will be briefly introduced and mainly the structure of titanate nanowires will be discused. The study of titanate nanowires was done by combination of powder X-ray diffraction and 3D rotation electron diffraction. The titanate nanowires were prepared by heating of titanate nanotubes up to 850 C. The structure of final product at 850 C depends on heating conditions and time of heating. We studied four samples - heated in air for 105 minutes, in air for 1000 minutes, in vacuum for 105 minutes and in vacuum for 1000 minutes. The transformation from anatase to rutile is observed in air and vacuum with increasing time of heating. Differences between samples heated in air and vacuum are that in air is observed sodium hexatitanate, anatase and rutile but sample heated in vacuum has only visible diffraction lines from anatase at the beganing of heating.

1. Bavykin DF. V.,Walsh F. C.: Titanate and titania nanotubes, synthesis, properties and application, RSC Publishing, 2010.
2. Morgado E., jr, de Abreu M. A. S., Pravia O. R. C., Marinkovic B. A., Jardim P. M., rizzo R.C., Araujo A.S.: A study on the structure and thermal stability of titanate nanotubes as a function of sodium content, Solid State Science, 8, 2006.
3. Yu J., Yu H., Cheng B., Trapalis C.: Effects of calcination temperature on the microstructures and photocatalytic activity of titanate nanotubes, Journal of Molecular Catalysis A, 249, 2006
4. Suzuki Y., Yoshikawa S.: Synthesis and thermal analysis of Tio2-deriveted nanotubes prepared by the hydrotherma method, Jounal Material Res., 19, 2004.